AIAA JOURNAL
Vol. 43, No. 8, August 2005

Experimental and Numerical Studies of Dilution Systems for Low-Emission Combustors

C. Prière* and L. Y. M. Gicquel†
Centre Européen pour la Recherche et la Formation Avancée en Calculs Scientifique, 31057 Toulouse, France
P. Gajan‡ and A. Strzelecki‡
ONERA, 31055 Toulouse, France
T. Poinsot§
Institut de Mécanique des Fluides de Toulouse, 31400 Toulouse, France
and
C. Bérat¶
Turbomeca, 64511 Bordes, France

Numerical and experimental investigations of eight isothermal jets in crossflow (eight-JICF) issuing radially in a round pipe are presented to assess advanced numerical approaches in industry-like configurations. The simulations are performed with large-eddy simulations (LES). Numerical issues such as grid resolution and physical issues such as injection of turbulence in the crossflow are addressed in this work. Detailed analyses of the LES predictions and comparisons with data underline the potential of the approach for industry-like configurations. Unsteady and averaged LES solutions of eight-JICF picture most of the single JICF features. The counter-rotating vortex pair, the wake vortices, and the shear-layer vortices are clearly identified in the experiment and by LES. Spectral analysis of the LES predictions reveals proper physical behavior of the different structures and good energy content distribution. Characteristic Strouhal numbers are within experimental scatter. Reynolds-averaged quantities (means and fluctuations) obtained by LES at several cross-stream locations are in good agreement with the experiment. Finally, jet trajectories and decay rates of crossflow velocities and jet air scalar concentration further assert the quality of the numerical results. This last analysis reveals that eight-JICF exhibits single free JICF behaviors but in a confined environment.

Introduction

NOWADAYS, the optimization of combustion performance and the reduction of pollutant emissions require considerable research efforts from the gas turbine industry. The basic objectives in combustor design are to achieve easy ignition, high combustion efficiency, and minimum pollutant emissions. Under such conditions two phenomena are to be controlled or avoided. First, the increase in NOx emissions as a result of the high levels of pressure and temperature needs to be restrained. Second, the feedback mechanism caused by the coupling between the flow and the flame can result in instabilities that originate in the periodic formation of inhomogeneous fuel pockets, the periodic shedding of large structures, and the amplification of the acoustic waves. These combustion instabilities[1–5] can yield dramatic damages or the failure of the combustor. Numerical methods are in that context very attractive alternatives to the expensive experimental setups required in such areas of research.

The aim of this work is to assess large-eddy simulations (LES)[6–10] for the design of the next-generation combustor. Contrary to the Reynolds-averaged Navier–Stokes (RANS) equations,[11–14] which are restricted to steady turbulent flows, LES offer numerous potential advantages and take into account combustion instabilities by solving for large flow structures while small-scale effects are modeled. The implications on the numerical predictions are of importance but still need to be illustrated and validated in the context of industrial applications. For information and illustrations of the potential of each method, the reader is referred to results obtained with state-of-the-art RANS[15–20] and LES.[21–26] Although more academic, these configurations[15–26] are of clear interest to this work.

This study constitutes a step further toward the full demonstration of LES for gas turbine engines with turbulent reacting multiphase flows. It addresses the problem of dilution jets in an industry-like configuration and aims at validating LES against experimental data gathered on a dedicated test rig located at ONERA (Toulouse). The geometry considered is typical of the dilution region of gas turbines and consists of eight isothermal jets in crossflow (JICF) issuing radially in a round pipe. It is hereinafter designated by eight-JICF, whereas the notation JICF will refer to a single jet in crossflow. Comprehensive experimental data for velocity and scalar concentration are gathered through advanced measurement techniques: laser Doppler anemometry (LDA), particle image velocimetry (PIV), particle laser-induced fluorescence (PLIF), and hot-wire anemometry. The effect of the grid resolution on the LES predictions is evaluated by performing the computations for two meshes: a coarse grid (grid M_1) and a fine grid (grid M_2). In complex geometries, the inlet conditions used for LES raise specific problems: a proper inlet condition should match the mean velocities but also the turbulent velocities and the acoustic impedance. In the present work, the effect of turbulence injection at the inlet is specifically tested by comparing simulations with and without turbulence injection through the main-stream inlet.

The paper starts with a brief presentation of the LES methodology followed by a description of the computational domain and the main flow characteristics. A section is then dedicated to the presentation of the LES predictions to be divided into three distinct subsections. First, a detailed presentation of the flow topology as predicted by

Received 24 November 2004; revision received 4 April 2005; accepted for publication 13 April 2005.

*Graduate Student, CFD Group, 42 Avenue G. Coriolis.
†Senior Researcher, CFD Group, 42 Avenue G. Coriolis.
‡Researcher, 2 Avenue Edouard Belin.
§Research Scientist, Allée du Professeur C. Soula. Member AIAA.
¶Director, Combustion Group, and Senior Expert, DT/CP/CTE, Avenue du Président Szydlowski.

LES and observed in free JICF is given. Second, a spectral analysis of the major flow features obtained in LES is compared to experimental measures obtained on eight-JICF. Finally, LES and experimental Reynolds-averaged fields of the means and fluctuations are investigated while jet trajectories and decay rates are compared to existing correlation functions. Assessments of the current work and perspectives on the application of LES to industry-like configurations are offered as concluding remarks.

Experimental Facility

The experimental rig of eight-JICF is shown in Fig. 1a. Dimensions and details of the experimental injection system are featured on Fig. 1b. Full optical access allows detailed analyses of the various flow phenomena. Experimental data consists of LDA, PIV, and PLIF fields taken at various cross-stream locations in the main pipe. Pointwise hot-wire anemometry measurements supplement the data set and are used for temporal assessments of the main flow structures. Main-pipe inlet velocity profiles measured with LDA complete the database.

Accuracy of the measured data is ensured through in-depth cross validations of the various diagnostics used. Experimental uncertainties are this way limited and clearly identified. Access to the experimental data is made available through inquiry to the MOLECULES work-package leader, C. Bérat (Turbomeca, Avenue du Président Szydlowski, 64511 Bordes, France), and the official consent of all project partners.

Numerical Simulations

Turbulent flows are known to contain large ranges of scales.[14,27,28] These scales, although not clearly defined mathematically, have been repeatedly evidenced in experimental measurements or direct numerical simulations (DNS) and LES.[29–31] The large-scale phenomena are usually associated with vortical structures whose dimensions are of the order of the domain size. The evolution of these scales is governed by the geometry of the combustion chamber, and they carry most of the turbulent kinetic energy. The smaller scales have on the other hand a relatively short range of influence and are believed to behave in a more universal way. Contrary to

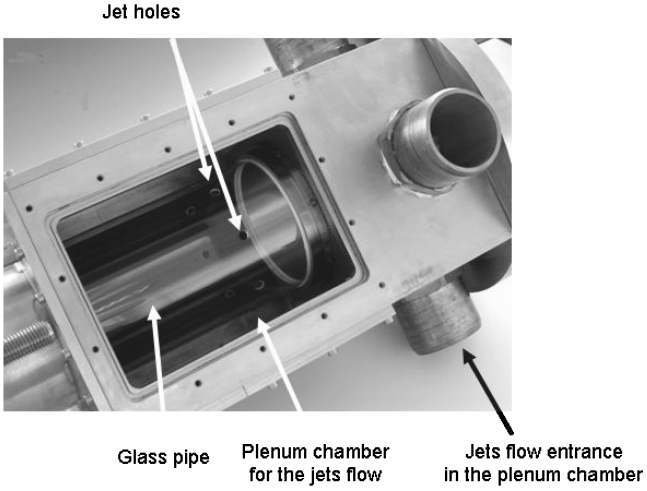

a)

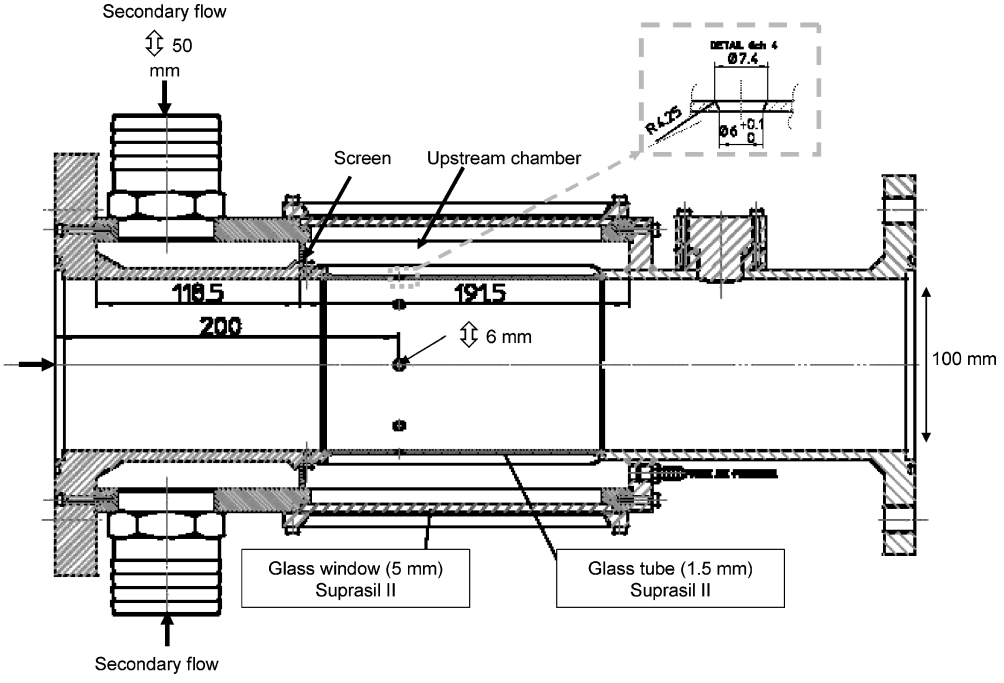

b)

Fig. 1 Experimental setup of ONERA: a) view of the experimental test section and b) its schematic representation.

RANS, in which all scales need to be modeled, LES filters out the small universal scales and aims at simulating only the dynamics of the large scales. The modeling is eased thanks to the universality of the physics governing the small scales. It yields an approach that is flexible and well suited to simulate cases encountered in the industry where large-scale phenomena are crucial.

Governing Equations

LES involves the spatial filtering operation[32]:

$$\overline{f(\boldsymbol{x},t)} = \int_{-\infty}^{+\infty} f(\boldsymbol{x}',t)\mathcal{G}(\boldsymbol{x}',\boldsymbol{x})\,\mathrm{d}\boldsymbol{x}' \tag{1}$$

where $\mathcal{G}$ denotes the filter function and $\overline{f(\boldsymbol{x},t)}$ is the filtered value of the variable $f(\boldsymbol{x},t)$. We consider spatially and temporally invariant and localized filter functions[32]; thus, $\mathcal{G}(\boldsymbol{x}',\boldsymbol{x}) \equiv G(\boldsymbol{x}'-\boldsymbol{x})$ with properties[32,33] $G(\boldsymbol{x}) = G(-\boldsymbol{x})$ and

$$\int_{-\infty}^{+\infty} G(\boldsymbol{x})\,\mathrm{d}\boldsymbol{x} = 1$$

In the mathematical description of compressible turbulent flows with species transport, the primary variables are the density $\rho(\boldsymbol{x},t)$, the velocity vector $u_i(\boldsymbol{x},t)$, the total energy $E(\boldsymbol{x},t) \equiv e_s + \frac{1}{2}u_i u_i$, and the mass fraction of species α, $Y_\alpha(\boldsymbol{x},t)$. The application of the filtering operation to the instantaneous transport equations yields[5]

$$\frac{\partial \bar{\rho}}{\partial t} + \frac{\partial}{\partial x_i}(\bar{\rho}\tilde{u}_i) = 0$$

$$\frac{\partial}{\partial t}(\bar{\rho}\tilde{u}_j) + \frac{\partial}{\partial x_i}(\bar{\rho}\tilde{u}_i\tilde{u}_j) = -\frac{\partial \bar{p}}{\partial x_j} + \frac{\partial \bar{\tau}_{jk}}{\partial x_k} - \frac{\partial}{\partial x_i}(\bar{\rho}\tilde{T}_{ij})$$

$$\frac{\partial}{\partial t}(\bar{\rho}\tilde{E}) + \frac{\partial}{\partial x_i}(\bar{\rho}\tilde{u}_i\tilde{E}) = -\frac{\partial \bar{q}_j}{\partial x_j} + \frac{\partial}{\partial x_j}[\overline{(\tau_{ij} - p\delta_{ij})u_i}]$$

$$- \frac{\partial}{\partial x_j}(\bar{\rho}\tilde{Q}_j) - \frac{\partial}{\partial x_j}(\bar{\rho}\tilde{T}_{ij}\tilde{u}_i)$$

$$\frac{\partial}{\partial t}(\bar{\rho}\tilde{Y}_\alpha) + \frac{\partial}{\partial x_i}(\bar{\rho}\tilde{u}_i\tilde{Y}_\alpha) = -\frac{\partial \bar{J}_i^\alpha}{\partial x_i} - \frac{\partial}{\partial x_i}\left(\bar{\rho}\tilde{F}_i^\alpha\right) \tag{2}$$

In Eq. (2), one uses the Favre-filtered variable[34] $\tilde{f} = \overline{\rho f}/\bar{\rho}$. The fluid follows the ideal-gas law $p = \rho RT$ and

$$e_s = \int_0^T C_p\,\mathrm{d}T - \frac{p}{\rho}$$

where e_s is the sensible energy, T stands for the temperature, and C_p is the fluid heat capacity at constant pressure. The viscous stress tensor, the heat diffusion vector, and the molecular transport of the passive scalar read, respectively,

$$\tau_{ij} = \mu\left(\frac{\partial u_i}{\partial x_j} + \frac{\partial u_j}{\partial x_i}\right) - \frac{2}{3}\mu\frac{\partial u_k}{\partial x_k}\delta_{ij}, \qquad q_i = -\lambda\frac{\partial T}{\partial x_i}$$

$$J_i^\alpha = -\rho D^\alpha \frac{\partial Y_\alpha}{\partial x_i} \tag{3}$$

In Eq. (3), μ is the fluid viscosity following Sutherland's law, λ the heat diffusion coefficient following Fourier's law, and D^α the species α diffusion coefficient (note that summation over repeated indices does not apply to Greek symbols). Variations of the molecular coefficients resulting from the unresolved fluctuations are neglected hereinafter so that the various expressions for the molecular coefficients become only a function of the filtered field.

The $\tilde{T}_{ij}$, $\tilde{Q}_i$, and $\tilde{F}_i$ terms correspond to the so-called subgrid-scale (SGS).[10,35] The unresolved SGS stress tensor $\tilde{T}_{ij}$ requires a subgrid turbulence model. Introducing the concept of SGS turbulent viscosity, most models read[36]

$$\tilde{T}_{ij} = (\widetilde{u_i u_j} - \tilde{u}_i\tilde{u}_j) = -2\nu_t\tilde{S}_{ij} + \tfrac{1}{3}\tilde{T}_{kk}\delta_{ij} \tag{4}$$

with

$$\tilde{S}_{ij} = \frac{1}{2}\left(\frac{\partial \tilde{u}_i}{\partial x_j} + \frac{\partial \tilde{u}_j}{\partial x_i}\right) - \frac{1}{3}\frac{\partial \tilde{u}_k}{\partial x_k}\delta_{ij} \tag{5}$$

In Eqs. (4) and (5), $\tilde{S}_{ij}$ is the resolved strain tensor and ν_t is the SGS turbulent viscosity. The wall adapting local eddy-viscosity (WALE) model[37] expresses ν_t as

$$\nu_t = (C_w\Delta)^2 \frac{\left(s_{ij}^d s_{ij}^d\right)^{\frac{3}{2}}}{(\tilde{S}_{ij}\tilde{S}_{ij})^{\frac{5}{2}} + \left(s_{ij}^d s_{ij}^d\right)^{\frac{5}{4}}}$$

$$\text{with} \qquad s_{ij}^d = \frac{1}{2}\left(\tilde{g}_{ij}^2 + \tilde{g}_{ji}^2\right) - \frac{1}{3}\tilde{g}_{kk}^2\delta_{ij} \tag{6}$$

In Eq. (6), Δ denotes the filter characteristic length and is approximated by the cubic root of the cell volume, C_w is the model constant ($C_w = 0.55$), and $\tilde{g}_{ij} = \partial\tilde{u}_i/\partial x_j$ is the resolved velocity gradient.

The SGS energy flux $\tilde{Q}_i = C_p(\widetilde{Tu_i} - \tilde{T}\tilde{u}_i)$ and the SGS scalar flux $\tilde{F}_i^\alpha = (\widetilde{u_i Y_\alpha} - \tilde{u}_i\tilde{Y}_\alpha)$ are respectively modeled by use of the eddy diffusivity concept with a turbulent Prandtl number $Pr_t = 0.9$ so that $\kappa_t = \nu_t C_p/Pr_t$ and species SGS turbulent diffusivity $D_t^\alpha = \nu_t/Sc_t^\alpha$, where Sc_t^α is the turbulent Schmidt number ($Sc_t^\alpha = 0.7$ for all α):

$$\tilde{Q}_i = -\kappa_t\frac{\partial \tilde{T}}{\partial x_i}, \qquad \tilde{F}_i^\alpha = -D_t^\alpha\frac{\partial \tilde{Y}_\alpha}{\partial x_i} \tag{7}$$

Note that $\tilde{T}$ is the modified filtered temperature and satisfies the modified filtered state equation (Refs. 30 and 38–40) $\bar{p} = \bar{\rho}R\tilde{T}$. Although the performances of the closures could be improved through the use of a dynamic formulation,[30,31,41–43] they are sufficient to investigate the present configuration.

In the context of industry-like configurations, the treatment of the wall turbulent boundary layer needs specific attention. With high-Reynolds-number flow (here $Re = 1.68 \times 10^5$), the turbulent boundary layer is thin compared to the length scales of the computational domain. To ensure a proper physical behavior of the near-wall solution in the context of LES, two approaches exist. The resolved LES requires a complete analysis of the grid resolution. With this approach, the inner-layer wall motions (essentially dominated by the quasi-streamwise vortices) must be sufficiently resolved; the filter and grid spacing must be of the order of δ_v (δ_v is the length scale of the viscous wall region). It can be estimated that the number of grid nodes required increases as $Re^{1.76}$ in the inner-wall region of the flow. For the outer layer, which contains the large-eddy scales, the grid resolution must resolve the turbulent kinetic energy and usually scales as $Re^{0.4}$. The resolved-LES approach usually implies too large computational costs for its direct application to high-Reynolds-number problems.[44] The second approach known as the approximate boundary condition methodology proposes to model the whole wall region. Numerous simplifications for the near-wall LES behavior have been investigated.[45–47] In this work, the log-law model[48–50] is assumed, and the wall stresses are modeled so as to mimic the wall effects on the global flow behavior. Note that in the implementation of this approach the wall boundary conditions use a nonzero velocity at the wall, which is determined locally using the log law and the information on the grid points directly above the wall nodes. Corrections on the temperature profile follow the same approach.

General Description of the Code

All computations are performed with a compressible Navier–Stokes code simulating unsteady flows on structured, unstructured, and hybrid grids (see http://www.cerfacs.fr). For the prediction of unsteady turbulence, different LES subgrid-scale models have been developed including the WALE model,[37] Eq. (6). The numerical discretization of the governing equations, Eqs. (2–7), uses a cell-vertex method,[51,52] and the discrete values of the conserved variables are stored at the cell vertices (or grid nodes). Despite the possible use of a numerical scheme offering third-order spatial and temporal

accuracies (TTGC scheme[53]), computations presented in this work are obtained with a second-order Lax–Wendroff scheme.

Simulations

Experiments for eight-JICF were performed for two values of the jet-to-mainstream momentum flux ratio J defined by

$$J = \frac{\rho_{\text{jet}} v_{\text{jet}}^2}{\rho_{\text{cf}} v_{\text{cf}}^2} \tag{8}$$

a low impulse case ($J = 4$) and a large one ($J = 16$). Both cases have been investigated with LES. For clarity, only the predictions obtained for $J = 16$ are presented in this work. (A similar topological behavior was obtained for the case $J = 4$.) The flow Reynolds number, based on the mainstream bulk velocity v_{cf} and the main duct diameter D, equals 1.68×10^5 for all cases. It ensures a high level of mixing and limited effects of the turbulent boundary layer. The jet Reynolds number based on the jet diameter d and jet bulk velocity v_{jet} equals 20.5×10^3 and 41×10^3 for $J = 4$ and 16, respectively. Note that because of the use of equal density fluids, the jet-to-mainstream momentum flux ratio J is equivalent to the square of the velocity ratio $R = v_{\text{jet}}/v_{\text{cf}}$. This flow parameter is hereinafter preferred to identify each case (i.e., $R = 4$ for $J = 16$ and $R = 2$ for $J = 4$).

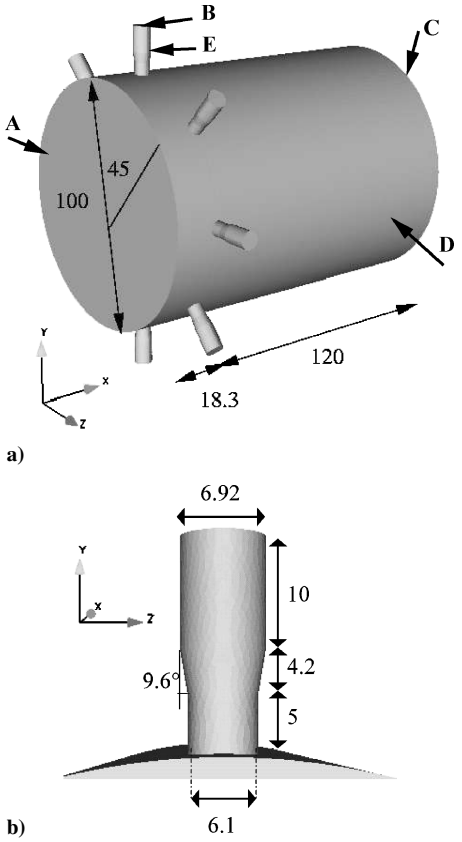

Fig. 2 Computational domain considered for LES of the isothermal jets in crossflow: a) patches representation and b) geometry of the jet injection system. All given distances are in millimeters.

Computational Domain

Figure 2 illustrates the computational domain retained for the eight-JICF experimental setup shown on Fig. 1. The length of the main pipe is 138.3 mm for a diameter of 100 mm. The jet inlet sections are located 18.3 mm downstream of the main pipe inlet and 120 mm upstream of the pipe outlet section. All jets are positioned 45 deg ($\pi/4$ radians) apart around the duct circumference. To reduce mesh size and computational cost, the injection system is modeled in LES by a straight injection system prolonged by a circular duct with dimensions identical to the one found in the experiment. The modeled section is circular (Fig. 2b) with a contraction ratio of $\beta = 0.811$. The jet inlet section has a diameter of 6.92 and 6.1 mm at the junction with the main pipe. The aim of this modification is to allow a proper acoustic treatment of the jet injection section in the main tube.[24–26]

The grid is fully unstructured and composed of tetrahedra. To control the total number of cells and reduce computational cost, mesh refinement is enforced where necessary. More specifically, injection areas, wall regions, and jet trajectories must be sufficiently resolved to capture the appropriate range of length scales. To facilitate refinement along the jet trajectory, a correlation function is used as a guideline within the computational domain. The guiding trajectory follows the expression for a single JICF[54] with low velocity ratio R:

$$x/d = (2.351 + 4/R)^{0.385}(1/R)^{2.6}(y/d)^{2.6} \tag{9}$$

In Eq. (9), x is the streamwise direction, y the wall-normal direction, and d the jet diameter. For the grid generation, the velocity ratio R in Eq. (9) is taken as four, irrespective of the case simulated. Although several laws for JICF trajectories are proposed in the literature, the dependency of the LES predictions on the correlation function to be used is not addressed in this work.

The two meshes as seen on Fig. 3 are used for all of the LES (i.e., $R = 2$ and 4). A coarse mesh M_1 and a finer one M_2 allow a clear assessment of the grid resolution (Table 1) and its impact on the time-averaged LES predictions. The minimum cell size is located in the region where the jet meets the mainstream flow and is the same for all jets. Computational effort corresponding to an increase of resolution from meshes M_1 to M_2 yields a factor of 1.625 in the total CPU time [as obtained on 32 O3800 processors of a SGI Power Challenge hosted by CINES (one flow-through time taking approximately eight CPU hours on mesh M_1)].

Table 1 Mesh characteristics

Grid	Total number of nodes	Total number of cells	Finer to larger cell ratio, m
M_1	240,000	1,200,000	$3.5 \times 10^{-4}/8.2 \times 10^{-3}$
M_2	400,000	2,100,000	$3.5 \times 10^{-4}/5.2 \times 10^{-3}$

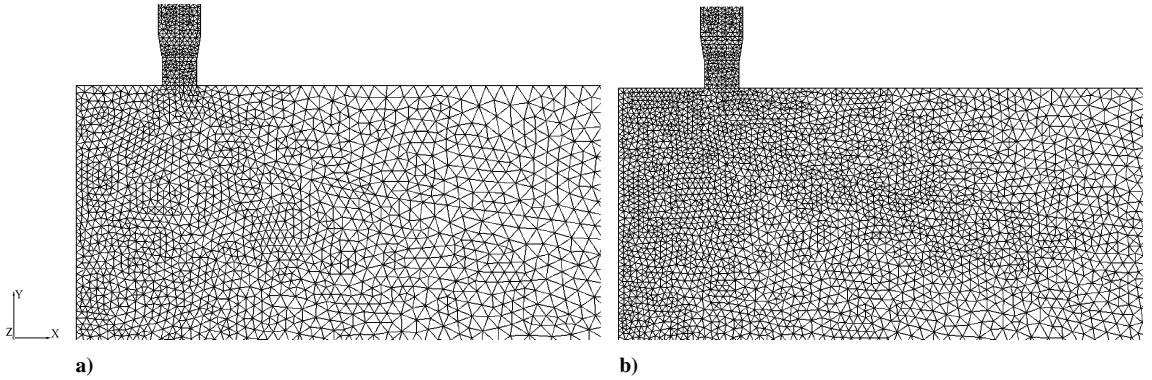

Fig. 3 Detailed view of the refinement used to generate a) the coarse mesh M_1 and b) the fine mesh M_2.

Table 2 Boundary conditions

Patch	BC	Imposed quantities	Approach	Relax	Acoustic property
A	Main inlet	$\tilde{u}, \tilde{v}, \tilde{w}, \tilde{T}, \tilde{Y}_\alpha$ with turbulence injection	Thompson[55]	500	Partially reflective
B	Jet inlets	$\tilde{u}, \tilde{v}, \tilde{w}, \tilde{T}, \tilde{Y}_\alpha$	Thompson[55]	500	Partially reflective
C	Main outlet	Freestream values	Poinsot and Lele[56]	0.5	Partially reflective
D	Main walls	Isothermal law of the wall	Thompson[55]	——	Reflective
E	Jet walls	Isothermal no-slip walls	Thompson[55]	——	Reflective

Boundary and Initial Conditions

When dealing with a fully compressible flow solver, special attention must be paid to the treatment of acoustics through the boundary conditions (BC). Acoustic waves can be generated through artificial transient phenomena because of the approximated initial solution and/or the wrong treatment of the BCs. For clarity, the set of BCs used in the LES is listed in Table 2. They are based on the method of characteristics.[55–57] All inlet conditions operate with the same type of BC (Table 2). For an inlet, the three components of the velocity vector, the temperature, and species mass fractions are imposed on the desired values through a relaxing parameter.[56] When this coefficient equals zero, the BC is acoustically nonreflective: exiting acoustic waves leave the domain freely, and no component is reinjected in the computational domain. When the coefficient is nonzero, the exiting acoustic wave is partially reflected and remains within the region of computation. Furthermore, zero relaxing coefficient can result in drifting mean quantities, and sufficiently large relaxation coefficients are needed so that mean values remain close to their target values.[58]

Turbulent pipe flow profiles are used to set the jet mean inlet velocity conditions (patch B in Fig. 2). The resulting bulk velocity respects the mass flux as measured by ONERA. In the case of a no-slip wall, a zero velocity is imposed at the wall, and the shape of the velocity profile issued at the intersection of the injection system and the main duct strongly depends on the grid resolution of the jet injection system. For this reason, outlet jet profiles found in LES might not reproduce experimental profiles at these locations. To diminish the differences and the potential implications on the flow predictions, no-slip isothermal ($\tilde{T} = 300$ K) walls are used in the jet injection systems with an increased grid resolution (patch E in Fig. 2). Other walls (patch D in Fig. 2) follow the isothermal wall law condition described earlier.

At the main duct inlet (patch A in Fig. 2) the values of $\tilde{u}$, $\tilde{v}$, and $\tilde{w}$ vary in time and space to reproduce the effect of an incoming turbulent field as observed in the experiment. The method in constructing the incoming turbulent signal is based on the random-flow-generation algorithm[59–61] itself based on early work.[62] The continuously homogeneous isotropic incoming field consists of a superposition of harmonic functions (50 modes projected in the three directions) with characteristic length scales prescribed by the user. Forcing the flow in such a way considerably accelerates the establishment of fully developed turbulent flows. It also ensures the presence of coherent perturbations not warranted when a pure white noise is used. Figure 4 depicts mainstream inlet profiles. All results are nondimensionalized by the crossflow velocity v_{cf}. Experimental measures are added as symbols. Measurement errors are for the mean field below 1% and around 4% for the fluctuating components. The actual responses of the code with and without injection of turbulence are, respectively, represented by the solid lines and the broken lines. All LES results agree with the measurements. Deviations of the LES fluctuating profiles from the mean target fluctuating profile imposed at the BC are caused by the unsteady nature of the incoming flow and the partially reflective condition.

The main duct outlet BC (patch C in Fig. 2) simulates a far-field state with given atmospheric conditions. This boundary condition is "soft"; the ingoing wave is computed as a difference between the LES solution at the boundary nodes and the reference state. A "relax" coefficient allows the absorbing of the acoustics making the condition partially reflective.

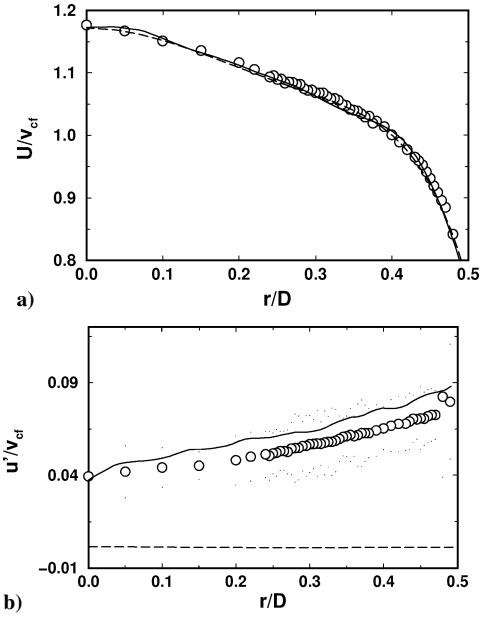

Fig. 4 Nondimensional profiles of a) the mean streamwise component of the velocity vector and b) its mean fluctuating component as functions of the nondimensional radius of the main duct *r/D*: – – –, case without turbulence injection; ——, case with turbulence injection; and ○, measurements.

All relax coefficients used for the LES of eight-JICF are listed in Table 2 and ensure low acoustic impedance of the boundary as verified by a posteriori validation of the incoming and outgoing acoustic signals.[58] Finally and to identify the mixing of the jets with the crossflow fluid, oxygen issued at the jet air inlet condition is differentiated from the oxygen of the crossflow air.

To proceed with the integration of the LES governing equations, an initial solution is needed. To diminish computational cost and artificial effects caused by the initial guess, a specific methodology is employed. Two steps are followed:

1) To achieve an approached solution in a reasonable time delay, the coarse mesh M_1 is first used to conduct the integration. To avoid spurious behaviors, the initial velocity is null and tends smoothly to the desired values through the inlet BCs.

2) The converged solution obtained in 1 is interpolated on the fine mesh M_2 to yield a new initial condition for proper integration of the LES equations.

Note that each step requires adaptation of the initial conditions toward physical solutions. Memory loss of the initial guesses is ensured by allowing the simulation to run for approximately one flow-through time before starting statistical sampling and analysis of the LES results.

Results and Discussion

Before the discussion on the LES and experimental flow topology, a brief introduction to the single JICF features is given. Jet visualizations of the eight-JICF LES predictions for the fine-grid M_2 and both velocity ratios follow. Vortex-shedding frequencies in the near-field region are investigated and gauged against experimental measurements. Then, mean velocity fields are presented

along with a qualitative assessment of the grid resolution and turbulence injection effects. Finally, jet trajectories and decay rates are assessed.

Flow Features

The single JICF configuration is widely used in many technical applications involving gas turbines, fuel injection, chimneys, etc. Compared to other shear flows (e.g., mixing layer, freejets), the JICF is the result of the complex three-dimensional interactions between the jet and the crossflow stream. It displays considerably more complexity with jet-like behavior in the near field and the far field. The literature proposes numerous works on the main vortical structures observed in several regions of the single JICF.[63–66] Four distinct vortical structures have been identified (see Fig. 5):

1) The jet shear-layer vortices that evolve on the jet column and whose vorticity is generated at the interface between the jet and the cross stream is the first structure. Such structures are the result of the Kelvin–Helmholtz instabilities of the annular shear layer.

2) The second structure is the horseshoe vortex system, which lies on the wall around the jet exit and which is quite similar to the structures observed for flows around a cylinder wall junction.[65] It also has been shown that the horseshoe relates to the shear-layer roll up and the shedding of vortices in the wake region.

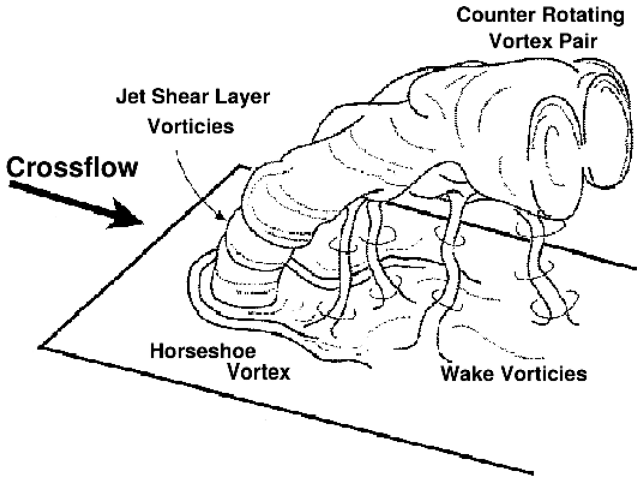

Fig. 5 Vortex system in a JICF.[63]

3) The wake structures form downstream the jet column and persist far downstream of the exit nozzle. The fluid comes from the wall boundary layer and sheds regularly from the leeward side of the jet. They can be detected in the wake region as ascending vortices. These very complex three-dimensional flow patterns are strongly influenced by the jet trajectory.

4) The counter-rotating vortex pair (CVP) is the dominant coherent structure of the JICF. It develops downstream and strongly depends on the boundary layer and plane wall region. The CVP plays a significant role in the far-field mixing.

In this paragraph, the single jet topology as obtained from the eight-JICF LES is presented for $R = 2$ and 4 with the help of four identification tools. Only the near-field region of one JICF out of the eight-JICF configuration is illustrated. It ensures that each JICF feature is not influenced by the neighboring JICFs. Figures 6a and 7a show isosurfaces of jet oxygen mass fraction; inner and outer jet boundary layers are defined by a jet oxygen mass fraction of 0.1. Jet air rapidly mixes with crossflow fluid to generate oxygen pockets. Such isosurfaces indicate that as R increases the jet integrity is clearly shortened in space, thus corresponding to enhanced mixing. The differences are asserted by Figs. 6b and 7b, where isosurfaces of low level of pressure are shown. Figures 6c and 7c illustrate the Q criterion. Based upon the second invariant of the velocity gradient tensor,[67] this criterion aims at detecting coherent structures in wall-bounded turbulent flows. Q is directly related to the pressure Laplacian, $\nabla^2 p = 2\rho Q$, for inviscid flows and can be interpreted as the source term of pressure in the Navier–Stokes equations. In Figs. 6d and 7d, the strong velocity gradients present near the wall prevent a clear identification of large-scale features through the streamwise component of the vorticity vector. This drawback is circumvented with the help of the Q criterion (Figs. 6c and 7c), which allows the identification of structures already illustrated with the isosurfaces of jet oxygen mass fraction.

All criteria show the jet column to deviate while it penetrates the crossflow. This pronounced feature of the JICF (Fig. 5) is present in the eight-JICF configuration. Shear-layer vortices can also be noticed for both velocity ratios. Traces of the CVP are also evidenced in the eight-JICF setup. The major difference observed between case $R = 4$ and case $R = 2$ is the penetration angle of each individual JICF and its transition toward a fully turbulent state. Strong similarities can, however, be found between the two cases as reported in previous works on JICF. Based on these observations, only $R = 4$ results are presented hereafter.

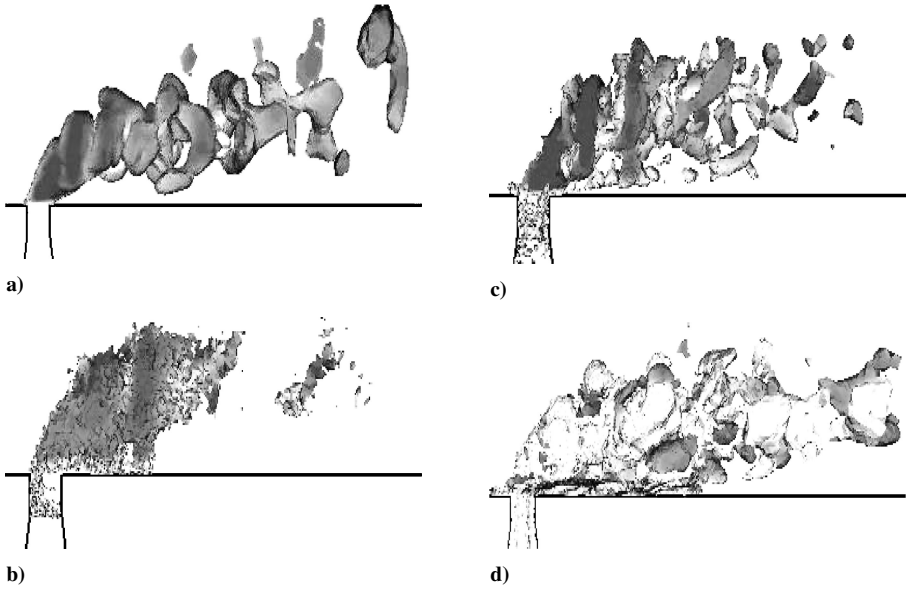

Fig. 6 Jet visualizations (grid M_2, case $R = 2$): a) isosurface of jet oxygen mass fraction $\tilde{Y}_{O_2} = 0.1$, b) isosurface of pressure $\bar{p} = 1.013$ bars, c) isosurface of Q criterion $Q = 9 \times 10^6 s^{-2}$, and d) isosurface of the streamwise component of the vorticity vector $\Omega_x = 3 \times 10^3 s^{-1}$. The isosurface is shaded with respect to the local value of the streamwise component of the velocity vector (light shades for low values and dark shades for large values).

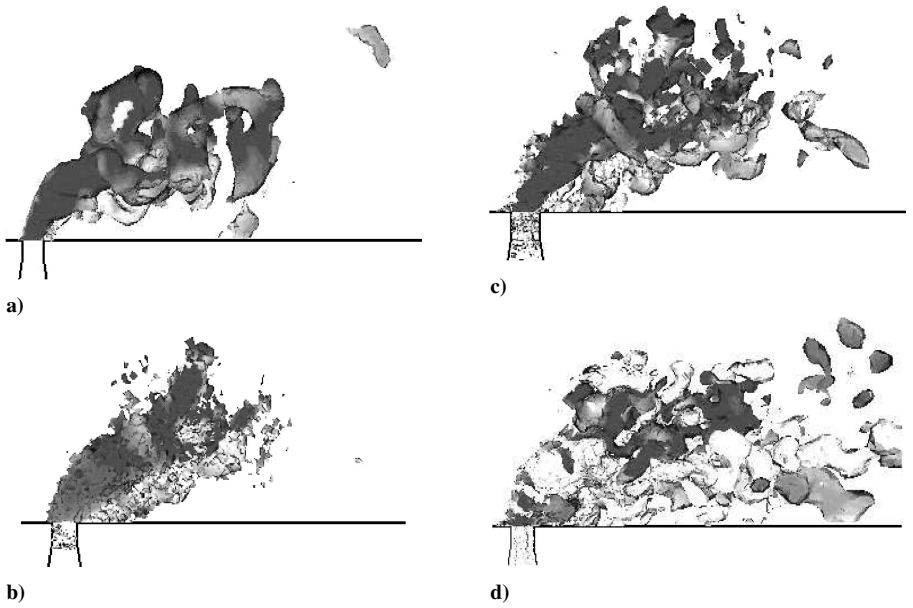

Fig. 7 Jet visualizations (grid M_2, case $R = 4$): a) isosurface of jet oxygen mass fraction $\tilde{Y}_{O_2} = 0.1$, b) isosurface of pressure $\bar{p} = 1.013$ bars, c) isosurface of Q criterion $Q = 9 \times 10^6 s^{-2}$, and d) isosurface of the streamwise component of the vorticity vector $\Omega_x = 3 \times 10^3 s^{-1}$. All isosurface is shaded with respect to the local value of the streamwise component of the velocity vector (light shades for low values and dark shades for large values).

Counter-Rotating Vortex Pair

The counter-rotating vortex pair (CVP) is a well known feature of the JICF configuration.[64,68] This coherent structure persists and keeps evolving even in the far-field region of the flow. It appears in steady and unsteady flow solutions and does not depend on the velocity ratio R and the flow Reynolds number Re. The CVP takes on an oval shape composed of two kidney-shaped counter-rotating vortices.

Figure 8 shows the CVP as observed in the eight-JICF LES predictions for one of the eight JICF. The normalized streamwise component of the vorticity vector Ω_x is shown at a) $x = 1d$ and b) $x = 2d$. Dark gray isolines correspond to clockwise rotations while light grey isolines identify counterclockwise rotations. The normalization of Ω_x by the planar maximum of $|\Omega_{x_0}|$ within the CVP (outside of the wall region) is performed so as to illustrate the downstream evolution of the CVP. Through this quantity the kidneylike structures are clearly observed in the LES predictions. The decay of the structure with the downstream direction is confirmed by LES (Figs. 8a and 8b). Built-in diffusive as well as dissipative forces of the system imply a decrease in the maximum of vorticity as the jet expands. The rotation of the two kidneylike structures induces creation of vorticity in the near-wall region and also decreases with the downstream direction.

Comparisons of the jet oxygen concentration given by an instantaneous LES solution with PIV particle traces in the CVP region (Fig. 9a) suggest that LES predictions and measurements do not necessarily depict well-defined and coherent structures at all instants and for all jets of eight-JICF. Gross agreement can be found, but no clear small- or large-scale pattern is identified in any jet. Finally, Fig. 9a underlines the unsteadiness of the flow evidenced through the asymmetries in the particle traces and the jet oxygen concentration. These asymmetries are not clearly evidenced by the averaged results (Fig. 9b). The qualitative good agreement between LES and measurements as illustrated in Fig. 9 highlights the clear potential of LES for industry-like computations.

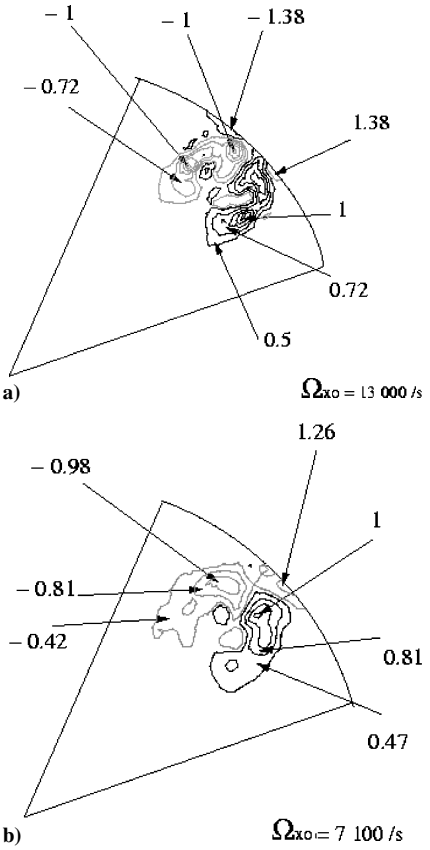

Fig. 8 Levels of the normalized streamwise vorticity Ω_x: a) plane $x = 1d$ and b) plane $x = 2d$.

Statistical Analysis

Instantaneous visualization of the LES predictions reveals the possibilities of the approach in predicting highly complex flows. Further analysis is however necessary to clearly assess LES for industrial applications. To do so, comparisons of the statistically averaged LES fields and corresponding experimental data are presented in this section. A frequency analysis of the various JICF structures identified earlier is exposed, followed by statistical moments. Finally, mixing of the jet air with the main flow is evaluated and gauged against existing correlation functions. LES animations point out that the instantaneous realizations of the JICF can deviate from their theoretical trajectory. The appearance of a weak coupling between neighboring jets is to be suspected in eight-JICF. Under these circumstances an independent treatment of all the JICF should be interpreted with care even if the timescales of the coupling appeared to be very long.

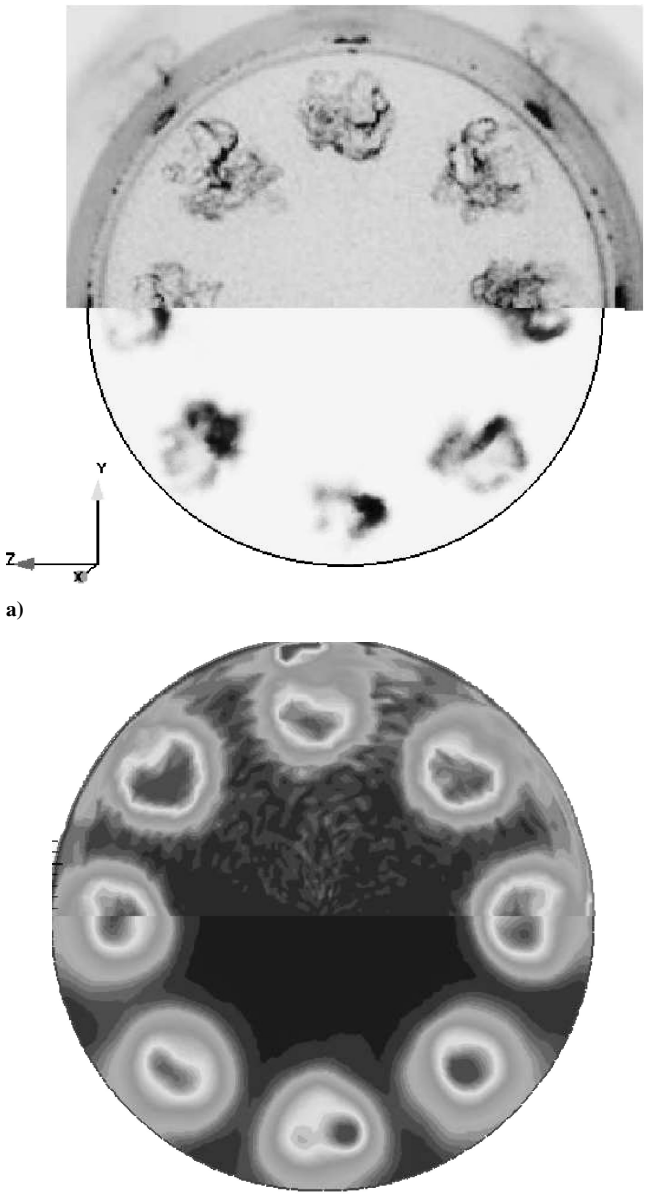

Fig. 9 Visualization of the CVPs as obtained from a) instantaneous and b) mean fields. Each picture displays experimental views of PIV particle traces (top) and LES views of jet oxygen concentration (bottom). Dark gray relates to large values of the concentrations and light gray corresponds to low values. The cross-stream plane used for visualization is located a) 1*d* and b) 5*d* downstream of the jet injection plane.

Vortex Shedding Frequencies

Vortex-shedding frequencies are of clear interest to the JICF users; large vortex structures can have a substantial impact on the mixing of the jets, which is one of the primary aims of the gas turbine industrial use of JICFs. In the experimental investigations, Fourier-spectral analysis of velocity signals (hot-wire anemometry) has been performed in two distinct regions: the wake and the jet shear layer. Probe locations have been determined based on visual investigations of the flow.

This paragraph presents the frequency acquisition method conducted on the numerical simulations. Wake and jet shear-layer vortices are studied at several probe locations where pronounced harmonics are found experimentally. To obtain a proper convergence of the spectral analysis, two hypotheses are needed for LES: first, the axisymmetry of the flow is assumed, although it has been pointed out that all jet penetrations are not strictly identical and independent; second, traveling in the downstream direction along the jet column, structures are supposed to be persistent, and vortex-shedding frequency is assumed to be equivalent for different probe locations in the regions of interest and before potential vortex pairings. Under these two assumptions, averaging of the individual Fourier spectrum is performed and compared to the measurements. The duration of the time series equals 37 ms (i.e., 6.7 convective times), and the sampling is performed at 6000 Hz. These time spans and sampling rates enable the capturing of most of the flow information. For the wake region, the analysis is based on the time series of the streamwise component of the velocity vector $\tilde{u}(\boldsymbol{x}, t)$ obtained on the fine grid M_2. The same approach is used in the shear layer with $\tilde{u}(\boldsymbol{x}, t)$ being sampled. The respective spectra are presented in terms of Strouhal numbers $Sr = fL_{\text{ref}}/U_{\text{ref}}$, where f is the frequency domain (in s^{-1}) and U_{ref} and L_{ref} are the reference velocity and reference length. Reference values need to be adjusted depending on the phenomena investigated. In this study, two regions are investigated: the wake region for which we take $U_{\text{ref}} = v_{\text{cf}}$ and $L_{\text{ref}} = d$ yielding $Sr_{v_{\text{cf}}} = fd/v_{\text{cf}}$, and the jet shear layer for which we have $U_{\text{ref}} = v_{\text{jet}}$ and $L_{\text{ref}} = d$ yielding $Sr_{v_{\text{jet}}} = fd/v_{\text{jet}}$.

The wake region is discussed first. Few references are found on this subject in JICF's literature. Characteristic Strouhal numbers found for the Kármán street behind a circular cylinder vary around $Sr_{v_{\text{cf}}} = 0.21$. JICF wake vortices were studied with the use of the smoke-wire technique[69] for several velocity ratios R. In the mentioned work, a degree of repeatability is found for the case $R = 4$ and varying crossflow Reynolds numbers ranging from 3.8×10^3 to 11.4×10^3. The experimental Strouhal number equals 0.13 for $R = 4$. Transitions to larger values occur around $R = 3$ and 6. In another experiment,[70] the problem is investigated for R ranging from 2 to 8 and a fixed cross-flow Reynolds equal to 8×10^3. The probe is located 2.7 jet diameters downstream of the injection point and $Sr_{v_{\text{cf}}} = 0.15$. In eight-JICF experiments, the velocity probe is placed 6 mm from the wall and 12 mm downstream of the jet axis. Treatment of the unsteady LES results is obtained with five probes placed in the wake region behind the injection zone and 2 mm apart (Fig. 10).

Vortex-shedding frequencies are computed for all of the eight JICF present in the flow (i.e., in all eight wake regions). Fast Fourier transforms obtained from the 40 points are averaged, and the corresponding LES Fourier spectrum is shown on Fig. 11a. Experimental results are illustrated on Fig. 11b. A broken line represents fast Fourier transforms of the streamwise component of the velocity vector $\tilde{u}(\boldsymbol{x}, t)$, and a continuous line represents a smoothed signal (after averaging over all of the realizations). LES predictions depict regular vortex shedding at one pronounced frequency corresponding to a Strouhal number of 0.18. Experiment yields a lower Strouhal number equal to 0.11 (Fig. 11b).

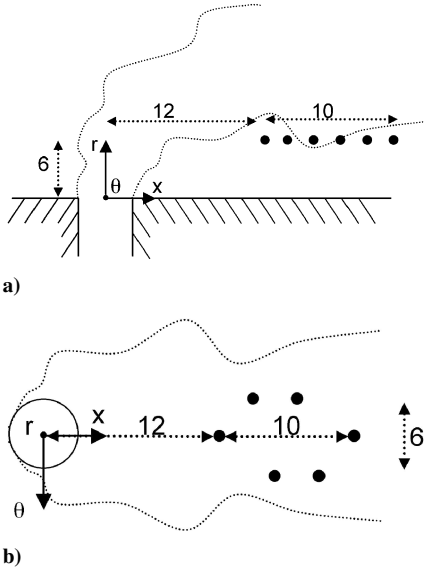

Fig. 10 Probe locations in the LES study of the wake region (dimensions are in millimeters): a) lateral view and b) top view.

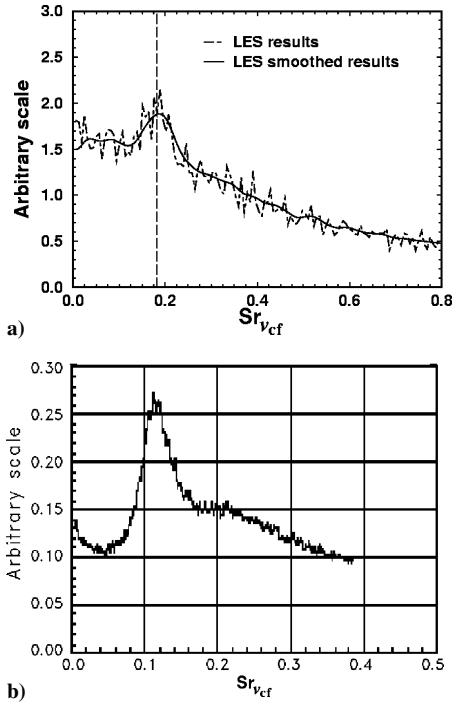

Fig. 11 Vortex-shedding frequencies analysis in the wake region: a) LES predictions and b) measurements.

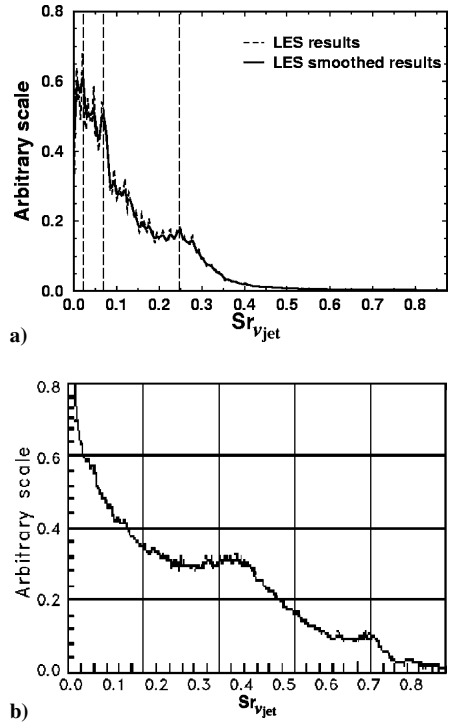

Fig. 13 Vortex-shedding frequencies analysis in the jet shear-layer region: a) LES predictions and b) measurements.

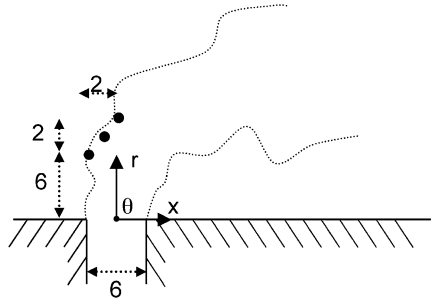

Fig. 12 Probe locations in the LES study of the jet shear-layer region (dimensions are in millimeters and shown for the plane $z = 0$).

Vortex-shedding frequencies of jet shear-layer structures have received more attention from researchers especially for acoustically excited transverse jets. Concerning unforced JICF, recent experiments[65] in both water and air suggest that periodic vortex ring roll-ups from the nozzle appear with a Strouhal number equal to 0.295. Another experiment points out the importance of the probe location.[71] The corresponding work reports different Strouhal number for a hot-wire probe positioned from approximately 1 to 1.5 jet diameters above the upstream edge of the jet exit. According to their observations, higher harmonics appear with increasing value of the cross-stream speed while keeping the velocity ratio constant ($R = 4$): $Sr_{v_{jet}} = 0.721$ with $v_{jet} = 4.8$ m/s and $Sr_{v_{jet}} = 0.828$ with $v_{jet} = 8$ m/s. The impact of the downstream location of the measuring point was also addressed.[72] To do so, the authors register velocity signals at three positions in the jet shear layer of a JICF with crossflow Reynolds number of 27.5×10^3 and a velocity ratio of 6. The reported Strouhal numbers are found to decrease with increasing downstream position. Finally, DNS assess the influence of the wall boundary layer.[73] The numerical experiments are performed for different velocity ratios and one nondimensionalized boundary-layer thickness $\delta_{BL}/d = 0.5$. For $R = 5.4$ their finding is $Sr_{v_{jet}} = 0.545$.

Figure 12 shows the three probe locations used to analyze LES predictions in the jet shear-layer region. The probes are positioned close to the upstream edge of the jet shear layer to help discern the large structure frequencies. In the experiment, the probe is placed 6 mm from the wall and 3 mm upstream of the jet axis.

LES predictions are compared against experimental data on Fig. 13. Spectrum's shape is qualitatively well reproduced. The high response observed at low frequencies probably corresponds to the CVP's formation. For both cases, the spectra seem to be masked by broadband behavior with no discernible dynamics in the range $0 < Sr_{v_{jet}} < 0.07$. This can be explained by the fact that probes are located slightly inside the jet and reveal internal details of the CVP's structure. For $0.07 < Sr_{v_{jet}} < 0.27$, the LES spectrum remains stable and reveals a small peak around a Strouhal number value of 0.24. The same general behavior is revealed in the experiment but over a much larger range, $0.2 < Sr_{v_{jet}} < 0.4$. A sustained plateau might also be visible in LES for $Sr_{v_{jet}} = 0.35$ and would correspond to the plateau at $Sr_{v_{jet}} = 0.7$ in the experiment. Finally, spectra go down sharply in the high-frequency range.

Many reasons can explain the differences found in the peak detections derived from LES predictions or experimental results. First, the jet injection system is different in LES (Fig. 2) and in the experiments (Fig. 1). Short ducts with contraction ratios equal to 0.811 are employed for LES to reduce the computational cost and to facilitate the treatment of the acoustic field at the jet inlet boundary. Geometric differences imply that jet-exit velocity profiles do not exactly represent the experimental conditions. Probe location is another difficulty as reported in previous works.[71,72] Most important, the grid resolution where the jet meets the crossflow along with the LES model used does not guarantee proper prediction of natural unstable modes of the shear layer. This implies pronounced Reynolds-number and LES model effects in the numerical approach. Note that such issues are commonly encountered in LES of transitioning flows and can hardly be solved without very dense grids and advanced subgrid models.[74–76] Such issues are, however, outside the scope of this work, and further investigations are being conducted on the subject. Finally, statistical convergence of the LES spectra cannot be as reported experimentally where thousands of spectra are available.

Despite the potential limitations of the proposed analysis, LES yields promising results even in the context of the industry-like configuration of this study. Indeed, the shape of the spectra is very well reproduced at several locations in the flow, indicating that the

physics governing LES is similar to the one reported by experiments. Peak Strouhal numbers are, however, poorly predicted by LES. Nevertheless, and despite the uncertainties associated with the flow configuration and the numerical approach, LES predictions are very encouraging.

Mean Fields

Having qualitatively assessed the potential of LES in reproducing the dynamics of industry-like configurations, a more quantitative analysis of the LES predictions needs to be performed. To fulfill this task, a statistical approach is adopted to construct averaged fields to be compared with ONERA's measurements. The averaging procedure corresponds to a Reynolds average of the instantaneous LES predictions. The time of integration is in this case approximately four flow-through times (based on the main duct bulk velocity and the computational length, i.e., 25 m/s and 138.3 mm). The importance of the mesh resolution on the first and second moments is assessed at this occasion. LES predictions obtained with and without turbulence injection are presented as well. The comparisons with experimental measurements are performed at three cross planes localized $2d$, $5d$, and $10d$ downstream of the jet injection plane.

The analysis focuses on the study of the mean and fluctuating streamwise component of the velocity predicted by LES. Results are nondimensionalized by the crossflow mean bulk velocity v_{cf}. The ordinate follows the duct radius (0 at the centerline and maximum at the duct wall) and is scaled by D, the main-pipe diameter. Figure 14 compares profiles of the nondimensional mean axial velocity against experimental data. Both grid resolutions (grids M_1 and M_2) are considered for the comparison of the LES with and without turbulence injection (denoted by TI on the graph). Very good agreement is found when comparing fine-grid LES predictions with the measured data. For all planes the jet penetration as well as the jet wake region is well reproduced. Effects caused by the increased mesh resolution in the jet near field are readily observed and result from three highly coupled phenomena. First, local increase of the mesh resolution allows one to enrich the LES flow solution with smaller and better resolved small-scale structures. The downstream JICF region is in turn more turbulent, and the large-scale energy content is better represented. Second, associated with this grid refinement is also a less dissipative LES. Improved levels of dissipation originate from a more efficient application of the LES model. The flow structures influenced by the model are closer to the required assumption for the use of the SGS model, that is, local isotropy. Third and last, smaller cell volumes usually go with decreased dissipative effects induced by the numerical scheme itself. Consequently and as observed in Fig. 14, the mean streamwise profiles are expected to be sharper (less diffused) in regions of improved energetic content, that is, $2d$ and $5d$. These results illustrate the necessity to properly resolve regions of importance for LES to yield good quality predictions. Iterative approach with adaptation of the local mesh resolution (as performed here) can therefore be required when no clear information can be inferred for the flow to be simulated. Finally, when TI is used, no significant change is observed when compared to other LES predictions. The intensity of the perturbations at the main inlet probably does not influence such turbulent shear flows. The importance of the crossflow turbulence in this context is not clear even though it is well known that such an approach can significantly improve the prediction in more academic configurations.

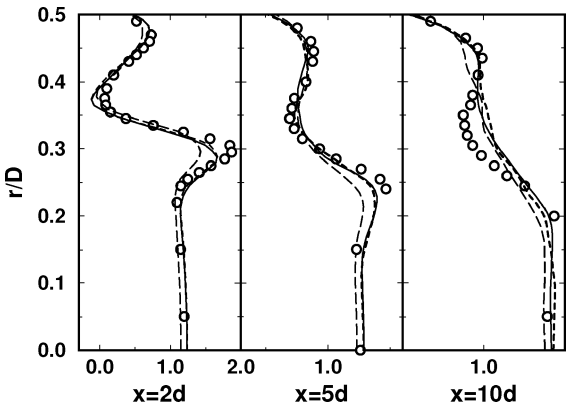

Fig. 14 Comparisons of the nondimensionalized mean streamwise component of the velocity vector u/v_{cf}, as obtained from the LES predictions and experimental measurements ○: – – –, grid M_1 without TI; · · · ·, grid M_2 without TI; and ——, grid M_2 with TI.

Figure 15 displays the mean axial component of the velocity vector for one-eighth of the cross-sectional planes located at $2d$, $5d$, and $10d$. Each LES field shown is time averaged over two flow-through times and spatially averaged over the eight jets to yield one section as obtained in the experiment. The color map is identical for both sets of results. At $x = 2d$, LES results depict a reasonably sized jet and a croissant-like shape linked to the passage of the vortex shear-layer structure. Going farther downstream, the overall agreement remains and confirms the observations of Fig. 14. Finally LES shows a slight asymmetry in the far field of the jet ($10d$ downstream the injection plane). Note that experimental measures are obtained for only half a jet and then symmetrized. Comparisons need therefore to be performed with care. Mean planar velocity vectors are also shown in Fig. 15 to illustrate the fluid motion in the $2d$, $5d$, and $10d$ planes. This latter quantity evidences the induced motion caused by the CVP.

The nondimensionalized fluctuation of the streamwise velocity component u'/v_{cf} is depicted on Fig. 16. LES predictions are in good agreement with measurements, and the profiles are very well represented: in the CVP's region, strong turbulent activity is found, as observed in the experiment at the three downstream locations. In the wall region, the fluctuation is well predicted by LES indicating the proper behavior of the wall model. The injection of turbulence at the inlet improves the predictions of u'/v_{cf} along the centerline of the main pipe ($r/D = 0$). Implications because of the mesh refinement are similar to the results observed for the mean streamwise component of the velocity vector (Fig. 15).

Although the identification of the various peak Strouhal numbers could not be predicted accurately, experimental mean values are still very well reproduced by LES. This further asserts the potential of LES for industrial applications and can be explained mainly by the reproduction in LES of the complex spatial and temporal physical phenomena observed experimentally.

Jet Trajectories and Decay Rates

JICF jet trajectories have received a lot of attention from researchers as well as from the industry. Often based on the locus of the maximum streamwise component of the velocity vector, the jet path can also be defined as the locus of the maximum jet scalar concentration in this same plane. Many experimental and theoretical works on free JICF indicate that the jet path can be expressed in self-similar variables for a large range of jet-to-mainstream momentum flux ratio (at least for free JICF). Some of the experimental correlations resulting from these previous works are given in Table 3 (Refs. 54 and 77–82).

LES results are gauged for both definitions against free JICF's experimental correlations as obtained for a velocity ratio of $R = 4$. Figures 17a and 17b, respectively, show jet paths in self-similar coordinates based on the streamwise component of the velocity vector and the scalar concentration maximum as functions of the nondimensionalized downstream directions. Agreement with experimental measurements on eight-JICF is very good and validates the LES results. When compared with analytical expressions, the present results are found to underpredict the proposed correlation functions over the entire length of the domain. Such results highlight the impact of the geometric differences between eight-JICF and a single free JICF. Confinement is expected to play a determining role in the latter while deliberately nonexistent in the former. Focusing on the criterion constructed from the velocity field (Fig. 17a), the initial jet deflection observed experimentally in the range $0 < x/d < 5$ and the downstream region $x/d > 10$ are very well replicated for both mesh resolutions (grids M_1 and M_2), with and without turbulence injection. LES and measures for eight-JICF are closer to the third

Table 3 Self-similar expressions for a free JICF's trajectories based on jet velocities and jet oxygen concentration

Author	Range of application	Correlation function
	Velocity-based trajectory	
Patrick[78a]	$6 < R < 50$	$y/d = R^{0.85}(x/d)^n$
Margason[77]	$2 < R < 10$	$x/d = (1/4)(1/R)^2(y/d)^3$
Kamotani and Greber[80]	$3.87 < R < 7.75$	$y/d = 0.89R^{0.94}(x/d)^{0.36}$
Chassaing et al.[54]	$2.37 < R < 6.35$	$x/d = (2.351 + 4/R)^{0.385}(1/R)^{2.6}(y/d)^{2.6}$
Fearn and Weston[81]	$3 < R < 10$	$y/d = 0.975R^{0.9085}(x/d)^{0.3385}$
Hasselbrink and Mungal[79b]	$1 \ll R$ (near field)	$y/Rd = [(2/c_{ej})(x/Rd)]^{\frac{1}{2}}$
	$1 \ll R$ (far field)	$y/Rd = [(3/c_{ew})(x/Rd)]^{\frac{1}{3}}$
	Scalar-concentration-based trajectory	
Patrick[78a]	$6 < R < 50$	$y/d = R^{0.85}(x/d)^n$
Kamotani and Greber[80]	$3.87 < R < 7.75$	$y/d = 0.73R^{1.04}(x/d)^{0.29}$
Karagozian[82]	Not specified	$y/d = 0.527R^{1.178}(x/d)^{0.314}$

[a]For Patrick's expression n is equal to 0.38 for the velocity and 0.34 for the concentration.
[b]For Hasselbrink's expression $c_{ej} = 0.32$ and $(3/c_{ew})^{(1/3)} = 1.6$.

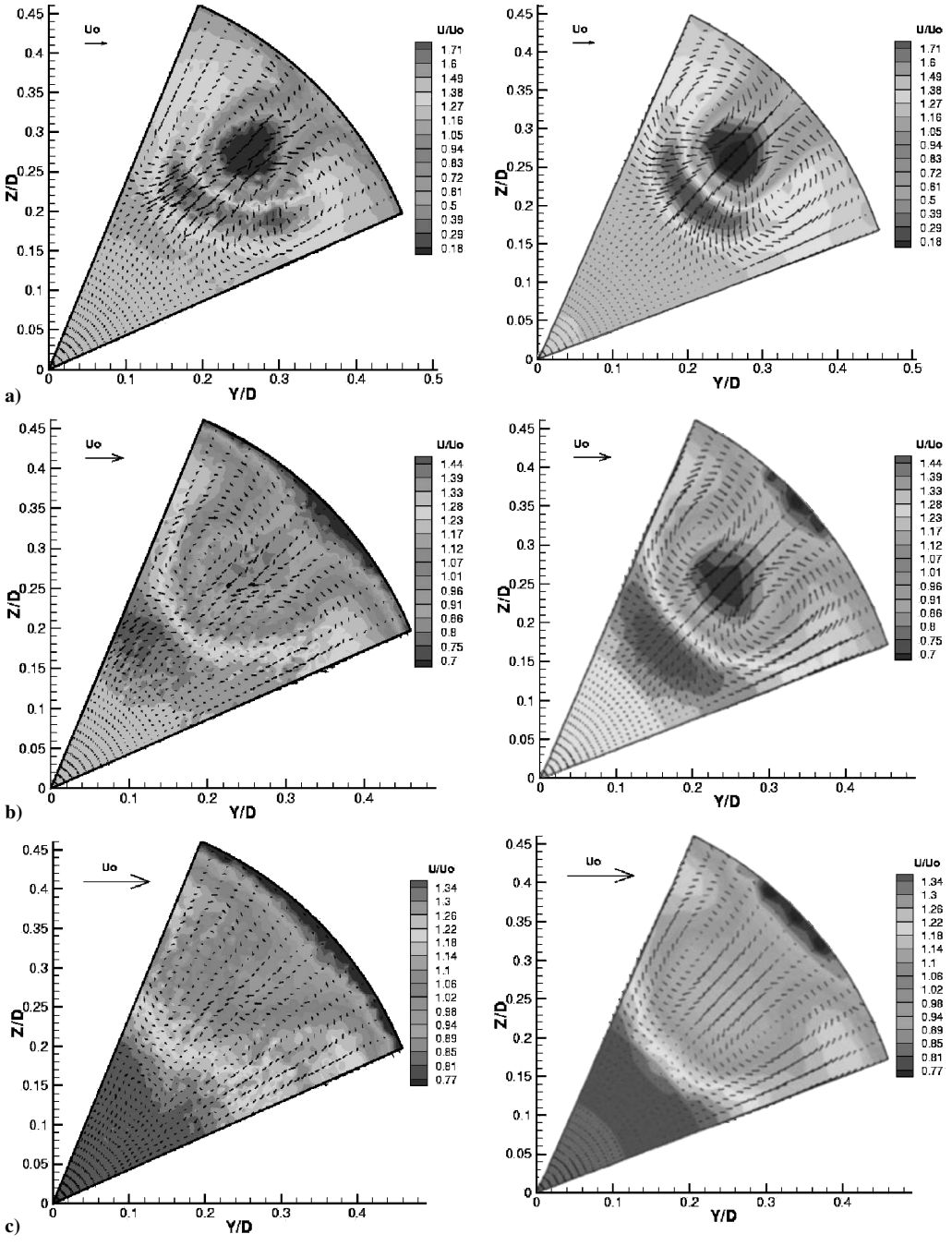

Fig. 15 Nondimensionalized fields of the mean axial component of the velocity vector u/v_{cf} obtained with LES (left column) and measured by ONERA (right column). The comparison is obtained for three downstream locations: a) $x = 2d$, b) $x = 5d$, and c) $x = 10d$.

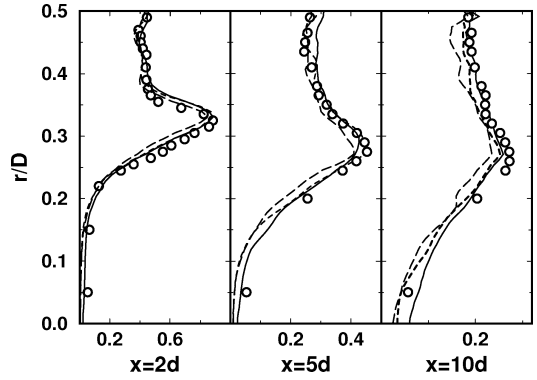

Fig. 16 Comparisons of the nondimensionalized fluctuation of the streamwise velocity component u'/v_{cf}, as predicted by LES and obtained in the experiment ○: – – –, grid M_1 without TI; · · · ·, grid M_2 without TI; and ——, grid M_2 with TI.

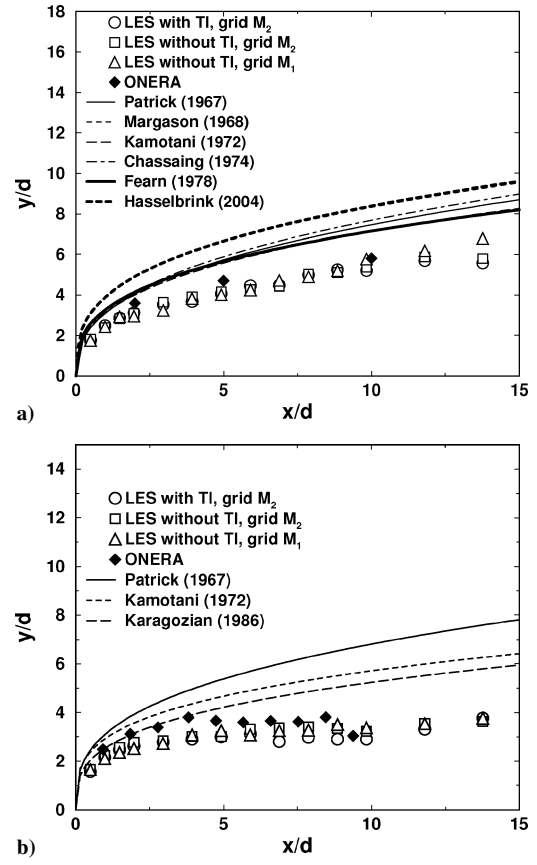

Fig. 17 Jet trajectories obtained by LES and the self-similar expressions given in Table 3: a) maximum of the streamwise component of velocity and b) maximum of scalar concentration.

and fifth correlation function.[77] For the jet oxygen maximum concentration (Fig. 17b) jet penetration is found to be closer to the first expression[78] for the scalar and LES reproduce the correlation in the near-field region. The mesh resolution and the turbulence injection do not seem to influence the jet trajectory.

Figures 18a and 18b, respectively, display the decays of the maximum streamwise component of velocity and the maximum jet oxygen scalar concentration along the respective trajectories shown in Fig. 17. The abscissa corresponds to the distance traveled along the jet trajectory from the injection point (denoted here by s). The decays are presented in a nondimensional form as indicated in the literature.[68,83] Figure 18 suggests power law decays as observed in free JICFs. In the near-field region, $\ell_n(s/Rd) < 1$, the maximum of velocity decreases to a -1 power as encountered for free turbulent jets. For $\ell_n(s/Rd) > 1$ (i.e., $s \approx 15d$), a transition occurs, and the decay rate tends toward the value of $-\frac{2}{3}$ as reported for free JICF.[79,84] These changes in slope are often related to the CVP, which increases the rate of mixing and the decay rate of the maximum value of the streamwise velocity component. Figure 18b corroborates the previous findings, especially for the case performed with turbulence injection. The near-field jet-like decay is less pronounced, and mixing seems accentuated when LES is closely analyzed. Modeling effects would need to be assessed to further validate the approach. The influence of the grid resolution is not significant in predicting the velocity and scalar concentration decay rates.

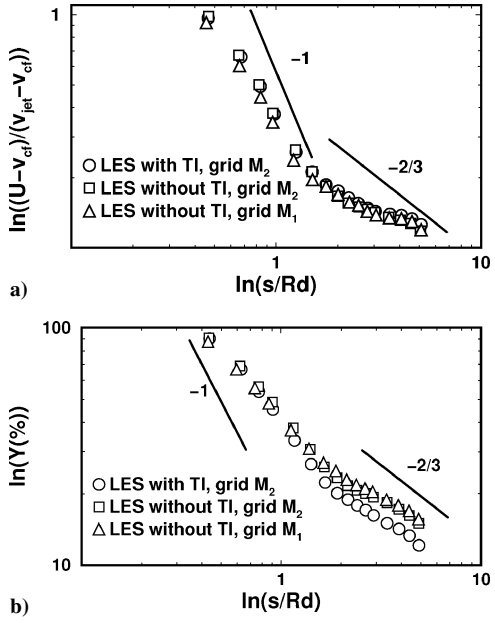

Fig. 18 Jet decay rates as predicted by LES: a) maximum streamwise component of the streamwise component of velocity and b) maximum scalar concentration, where ——, decay laws.

Conclusions

This work assesses the potential of the large-eddy simulations (LES) approach in the context of an industry-like configuration. The study focuses on a typical dilution zone in gas turbine geometries. More specifically LES are performed for eight isothermal jets in crossflow (JICF) issuing radially in a round pipe. Experimental measurements and detailed diagnostics allow a clear assessment of the LES predictions. Special attention is devoted to the mesh resolution and the effect of turbulence injection in the crossflow. The influence of the grid resolution and the addition of turbulence at the main duct inlet do not imply significant changes in the predictions. Spectral analysis of the various time-dependent structures usually present in a free JICF proves LES to be a very powerful tool to predict unsteady behavior. Indeed, large vortical structures such as the counter-rotating vortex pairs (CVPs), the shear-layer vortices, and the wake vortices are readily observed in LES. Peak Strouhal numbers are within the experimentally reported values. Experimental means (first moments and fluctuations) are very well reproduced at various locations of the main duct pipe. Finally, jet trajectories and decay rates are found to be in agreement with experimental measures. Comparisons with experimental and various existing correlation functions for free JICF indicate that confinement effects are present in the studied geometry and further assert the overall potential of the LES approach for industrial applications.

Acknowledgments

This work is funded by the European Community through project MOLECULES (Modeling of Low Emissions Combustor Using Large Eddy Simulations, GR4D-CT-2000-00402) and under the work-package coordination of Turbomeca (C. Bérat) and project coordination of Rolls-Royce Deutschland (R. Eggels). The authors are indebted to the precious comments of the various MOLECULES

partners as well as G. Mungal. Computer support was granted by the Centre Informatique National de l'Enseignement Supérieur, Montpellier, France, under Project fac2554.

References

[1]Rayleigh, L., "The Explanation of Certain Acoustic Phenomena," *Nature*, Vol. 18, No. 8, 1878, pp. 319–321.

[2]Putnam, A. A., *Combustion Driven Oscillations in Industry*, American Elsevier, New York, 1971, pp. 156–208.

[3]Strahle, W., "Combustion Noise," *Energy and Combustion Science*, Vol. 4, No. 5, 1978, pp. 157–176.

[4]Williams, F. A., *Combustion Theory*, Benjamin Cummings, New York, 1985.

[5]Poinsot, T., and Veynante, D., *Theorical and Numerical Combustion*, R. T. Edwards, Flourtown, PA, 2001.

[6]Ferziger, J. H., "Large Eddy Simulations of Turbulent Flows," *AIAA Journal*, Vol. 15, No. 9, 1977, pp. 1261–1267.

[7]Lesieur, M., and Métais, O., "New Trends in Large-Eddy Simulations of Turbulence," *Annual Review of Fluid Mechanics*, Vol. 28, 1996, pp. 42–82.

[8]Mason, P. J., "Large-Eddy Simulation: A Critical Review of the Technique," *Quarterly Journal of the Royal Meteorological Society*, Vol. 120, No. 515, 1994, pp. 1–26.

[9]Rogallo, R. S., and Moin, P., "Numerical Simulation of Turbulent Flows," *Annual Review of Fluid Mechanics*, Vol. 16, 1984, pp. 99–137.

[10]Sagaut, P., *Large Eddy Simulation for Incompressible Flows*, Springer-Verlag, New York, 2001.

[11]Launder, B. E., and Spalding, D. B., *Mathematical Models of Turbulence*, Academic Press, London, 1972.

[12]Pope, S. B., *Turbulent Flows*, Cambridge Univ. Press, Cambridge, England, UK, 2000.

[13]Chassaing, P., *Turbulence en Mécanique des fluides. Analyse du Phénomène en vue de sa Modélisation à l'Usage de l'Ingénieur*, Polytech, Toulouse, France, 2000.

[14]Tennekes, H., and Lumley, J. L., *A First Course in Turbulence*, MIT Press, Cambridge, MA, 1972.

[15]Chiu, S. H., Roth, K. R., Margason, R. J., and Jin, T., "A Numerical Investigation of a Subsonic Jet in Cross Flow," *Computational and Experimental Assessment of Jets in Cross Flow*, CP-534, AGARD, 1993.

[16]Alvarez, J., Jones, W. P., and Seoud, R., "Predictions of Momentum and Scalar Fields in a Jet in Cross Flow Using First and Second Order Turbulence Closures," *Computational and Experimental Assessment of Jets in Cross Flow*, CP-534, AGARD, 1993.

[17]Claus, R. W., and Wanka, S. P., "Multigrid Calculations of a Jet in Crossflow," *Journal of Propulsion and Power*, Vol. 8, No. 2, 1992, pp. 423–431.

[18]Kim, S. W., and Benson, T. J., "Calculation of a Circular Jet in Crossflow with Multiple-Time-Scale Turbulence Model," *International Journal of Heat and Mass Transfer*, Vol. 35, No. 10, 1992, pp. 2357–2365.

[19]Demeuren, A. O., "Characteristics of Three-Dimensional Turbulent Jets in Crossflow," *International Journal of Engineering Science*, Vol. 31, 1993, pp. 899–913.

[20]Rudman, M., "Numerical Simulation of a Jet in Crossflow," *International Colloqium on Jets, Wakes and Shear Layers*, CSIRO, Melbourne, Australia, 1994.

[21]Jones, W. P., and Wille, M., "Large Eddy Simulation of a Round Jet in a Cross-Flow," *Engineering Turbulence Modeling and Experiments 3*, edited by W. Rodi and G. Bergeles, Elsevier, 1996, pp. 199–208.

[22]Yuan, L. L., Street, R. L., and Ferziger, J. H., "Trajectory and Entrainment of a Round Jet in Crossflow," *Physics of Fluids*, Vol. 10, No. 9, 1998, pp. 2323–2335.

[23]Yuan, L. L., Street, R. L., and Ferziger, J. H., "Large Eddy Simulations of a Round Jet in Crossflow," *Journal of Fluid Mechanics*, Vol. 379, 1999, pp. 71–104.

[24]Schlüter, J. U., Angelberger, C., Schönfeld, T., and Poinsot, T., "LES of Jets in Crossflow and Its Applications to a Gas Turbine Burner," *Turbulence and Shear Flow Phenomena*, edited by S. Banerjee and J. K. Eaton, Vol. 1, Begell House, New York, 1999, pp. 71–76.

[25]Schlüter, J. U., and Schönfeld, T., "LES of Jets in Crossflow and Its Application to a Gas Turbine Burner," *Flow, Turbulence and Combustion*, Vol. 65, No. 2, 2000, pp. 177–203.

[26]Prière, C., Gicquel, L. Y. M., Kaufmann, A., Krebs, W., and Poinsot, T., "LES of Mixing Enhancement: LES Predictions of Mixing Enhancement for Jets in Cross-Flows," *Journal of Turbulence*, Vol. 5, No. 1, 2004, p. 5.

[27]Hinze, J. O., *Turbulence*, Series in Mechanical Engineering, McGraw–Hill, New York, 1975.

[28]Batchelor, G. K., *The Theory of Homogeneous Turbulence*, Cambridge Univ. Press, New York, 1967.

[29]Blaisdell, G. A., Mansour, N. N., and Reynolds, W. C., "Compressibility Effects on the Growth and Structure of Homogeneous Turbulent Shear Flows," *Journal of Fluid Mechanics*, Vol. 256, 1993, pp. 443–485.

[30]Moin, P., Squires, K., Cabot, W., and Lee, S., "A Dynamic Subgrid-Scale Model for Compressible Turbulence and Scalar Transport," *Physics of Fluids*, Vol. A3, Nov. 1991, pp. 2746–2757.

[31]Lilly, D. K., "A Proposed Modification of the Germano Sub-Grid Closure Method," *Physics of Fluids*, Vol. A4, No. 3, 1992, pp. 633–635.

[32]Aldama, A. A., *Filtering Techniques for Turbulent Flow Simulations*, Springer-Verlag, New York, 1990.

[33]Vreman, B., Geurts, B., and Kuerten, H., "Realizability Conditions for the Turbulent Stree tensor in Large-Eddy Simulation," *Journal of Fluid Mechanics*, Vol. 278, 1994, p. 351.

[34]Favre, A., "Statistical Equations for Turbulent Gases," *Problems of Hydrodynamics and Continuum Mechanics*, Society for Industrial and Applied Mathematics, Philadelphia, 1969, pp. 231–266.

[35]Ferziger, J. H., "Higher Level Simulations of Turbulent Flows," Stanford Univ., Dept. of Mechanical Engineering, Stanford Univ., Technical Rept. TF-16, Stanford, CA, March 1981.

[36]Smagorinsky, J., "General Recirculation Experiments with the Primitive Equations. I. The Basic Experiment," *Monthly Weather Review*, Vol. 91, No. 3, 1963, pp. 99–164.

[37]Nicoud, F., and Ducros, F., "Subgrid-Scale Stress Modelling Based on the Square of Velocity Gradient Tensor," *Flow, Turbulence and Combustion*, Vol. 62, No. 3, 2000, pp. 183–200.

[38]Erlebracher, G., Hussaini, M. Y., Speziale, C. G., and Zang, T. A., "Towards the Large Eddy Simulation of Turbulent Flows," *Journal of Fluid Mechanics*, Vol. 238, 1992, p. 155.

[39]Ducros, F., Comte, P., and Lesieur, M., "Large-Eddy Simulation of Transition to Turbulence in a Boundary Layer over an Adiabatic Flat Plate," *Journal of Fluid Mechanics*, Vol. 326, 1996, pp. 1–36.

[40]Comte, P., Métais, O., and Ferziger, J. H., *New Tools in Turbulence Modelling. Vortices in Incompressible LES and Non-Trivial Geometries*, Course of Ecole de Physique des Houches, Springer-Verlag, France, 1996.

[41]Germano, M., "Turbulence: The Filtering Approach," *Journal of Fluid Mechanics*, Vol. 238, 1992, pp. 238–325.

[42]Meneveau, C., Lund, T., and Cabot, W., "A Lagrangian Dynamic Subgrid-Scale Model of Turbulence," *Journal of Fluid Mechanics*, Vol. 319, 1996, pp. 353–385.

[43]Ghosal, S., Lund, T., Moin, P., and Akselvoll, K., "A Dynamic Localization Model for Large Eddy Simulation of Turbulent Flow," *Journal of Fluid Mechanics*, Vol. 286, 1995, pp. 229–255.

[44]Piomelli, U., Ferziger, J. H., Moin, P., and Kim, J., "New Approximate Boundary Conditions for Large-Eddy Simulations of Wall-Bounded Flows," *Physics of Fluids*, Vol. A, No. 1, 1989, pp. 1061–1068.

[45]Deardorff, J. W., "A Numerical Study of Three-Dimensional Turbulent Channel Flow at Large Reynolds Numbers," *Journal of Fluid Mechanics*, Vol. 41, 1970, pp. 453–480.

[46]Chapmann, D. R., "Computational Aerodynamics, Development and Outlook," *AIAA Journal*, Vol. 17, No. 9, 1979, pp. 1293–1313.

[47]Piomelli, U., and Balaras, E., "Wall Models for Large-Eddy Simulations," *Annual Review of Fluid Mechanics*, Vol. 34, 2002, pp. 349–374.

[48]Shumann, U., "Subgrid Scale Model for Finite Difference Simulations in Plane Channels and Annuli," *Journal of Computational Physics*, Vol. 18, Aug. 1975, pp. 376–404.

[49]Prandtl, L., "Uber die Ausgebildete Turbulenz," *Zeitschrift fur Angewandte Mathematik und Mechanik*, Vol. 5, 1925, pp. 136–139.

[50]von Kármán, T., "Progress in the Statistical Theory of Turbulence," *Proceedings of the National Academy Sciences*, Vol. 34, No. 11, 1948, pp. 530–539.

[51]Schonfeld, T., and Rudgyard, M. A., "Steady and Unsteady Flows Simulations Using the Hybrid Flow Solver avbp," *AIAA Journal*, Vol. 11, No. 37, 1999, pp. 1378–1385.

[52]Rudgyard, M. A., and Schonfeld, T., *A Modular Approach for Computational Fluid Dynamics*, Toulouse, France, 1994.

[53]Colin, O., and Rudgyard, M. A., "Development of High-Order Taylor-Galerkin Schemes for LES," *Journal of Computational Physics*, Vol. 162, No. 2, 2000, pp. 338–371.

[54]Chassaing, P., George, J., Claria, A., and Sanares, S., "Physical Characteristics of Subsonic Jets in a Cross-Stream," *Journal of Fluid Mechanics*, Vol. 62, No. 1, 1974, pp. 41–64.

[55]Thompson, K. W., "Time Dependent Boundary Conditions for Hyperbolic Systems," *Journal of Computational Physics*, Vol. 68, Jan. 1987, pp. 1–24.

[56]Poinsot, T., and Lele, S., "Boundary Conditions for Direct Simulations of Compressible Viscous Flows," *Journal of Computational Physics*, Vol. 101, No. 1, 1992, pp. 104–129.

[57]Nicoud, F., and Poinsot, T., "Boundary Conditions for Compressible Unsteady Flows," *Artificial Boundary Conditions at Interfaces*, edited by L. Halpern, F. Nataf, and L. Tourrette, Novascience, New York, 2001, pp. 78–108.

[58] Selle, L., Nicoud, F., and Poinsot, T., "Actual Impedance of Nonreflecting Boundary Conditions: Implications for Computations of Resonators," *AIAA Journal*, Vol. 42, No. 5, 2004, pp. 958–964.

[59] Smirnov, A., Shi, S., and Celik, I., "Random Flow Simulations with a Bubble Dynamics model," American Society of Mechanical Engineers, FEDSM2000 11215, June 2000.

[60] Van Kalmthout, E., Poinsot, T., and Candel, S., "Turbulence, Théorie et Simulations Directes," Laboratoire EM2C, TR/CFD/95/39, Ecole Centrale de Paris, Paris, 1995.

[61] Askelvoll, K., and Moin, P., *Large Eddy Simulation of Turbulent Confined Co-Annular Jets and Turbulent Flow over Backward Facing Step*, Dept. of Mechanical Engineering, Turbulent Flows Series, Stanford Univ., Stanford, CA, 1995, Chap. TF-63.

[62] Kraichnan, R., "Diffusion by Random Velocity Field," *Physics of Fluids*, Vol. 13, 1970, pp. 22–31.

[63] Fric, T. F., and Roshko, A., "Structure in the Near Field of the Transverse Jet," *Proceedings of the 7th Symposium on Turbulent Shear Flows*, Vol. 1, Pennsylvania State Univ., University Park, PA, 1989, pp. 6.4.1–6.4.6.

[64] Andreopoulos, J., and Rodi, W., "Experimental Investigation of Jets in a Crossflow," *Journal of Fluid Mechanics*, Vol. 138, 1984, pp. 93–127.

[65] Kelso, R. M., and Lim, T. T., "An Experimental Study of Round Jets in Cross-Flow," *Journal of Fluid Mechanics*, Vol. 306, 1996, pp. 111–114.

[66] Rivero, A., Ferré, J. A., and Giralt, F., "Organized Motions in a Jet in Crossflow," *Journal of Fluid Mechanics*, Vol. 444, 2001, pp. 117–149.

[67] Hunt, J. C. R., Wray, A. A., and Moin, P., "Eddies, Streams; and Convergence Zones in Turbulent Flows," *Proceedings of the Summer Program*, NASA Center for Turbulence Research, CTR-S88, 1988.

[68] Smith, S. H., and Mungal, M. G., "Mixing, Structure and Scaling of the Jet in Crossflow," *Journal of Fluid Mechanics*, Vol. 357, 1997, pp. 83–122.

[69] Fric, T. F., and Roshko, A., "Vortical Structure in the Wake of a Transverse Jet," *Journal of Fluid Mechanics*, Vol. 279, 1994, pp. 1–47.

[70] Moussa, Z. M., Trischka, J. W., and Eskinazi, S., "The Near Field in the Mixing of a Round Jet with a Cross-Stream," *Journal of Fluid Mechanics*, Vol. 80, 1977, pp. 49–80.

[71] Shapiro, S., King, J., Karagozian, A. R., and M'Closkey, R., "Optimization of Controlled Jets in Crossflow," AIAA Paper 2003-634, Jan. 2003.

[72] Narayanan, S., Barooah, P., and Cohen, J. M., "Dynamics and Control of an Isolated Jet in Crossflow," *AIAA Journal*, Vol. 41, No. 12, 2003, pp. 2316–2330.

[73] Cortelezzi, L., and Karagozian, A. R., "On the Formation of the Counter-Rotating Vortex Pair in Transverse Jets," *Journal of Fluid Mechanics*, Vol. 446, 2001, pp. 347–373.

[74] Li, Y., and Meneveau, C., "Analysis of Mean Momentum Flux in Subgrid Models of Turbulence," *Physics of Fluids*, Vol. 16, No. 9, 2004, pp. 3483–3486.

[75] Jiménez, J., and Moser, R. D., "Large-Eddy Simulations: Where Are We and What Can We Expect?," *AIAA Journal*, Vol. 38, No. 4, 2000, pp. 605–612.

[76] Liu, S., Katz, J., and Meneveau, C., "Evolution and Modeling of Subgrid Scales During Rapid Straining of Turbulence," *Journal of Fluid Mechanics*, Vol. 387, 1999, pp. 281–320.

[77] Margason, R. J., "Fifty Years of Jet in Crossflow Research. In Computational and Experimental Assessment of Jets in Crossflow," AGARD, CP-534, Nov. 1993.

[78] Patrick, M. A., "Experimental Investigation of the Mixing and Penetration of a Round Turbulent Jet Injected Perpendicularly into a Transverse Stream," *Transactions of the Institute of Chemical Engineers*, Vol. 45, 1967, pp. 16–31.

[79] Hasselbrink, E. F., and Mungal, M. G., "Transverse Jets and Jet Flames. Part I. Scaling Laws for Strong Transverse Jets," *Journal of Fluid Mechanics*, Vol. 443, 2001, pp. 1–25; also Part II, *Journal of Fluid Mechanics*, Vol. 443, 2001, p. 27.

[80] Kamotani, Y., and Greber, I., "Experiments on a Turbulent Jet in Crossflow," *AIAA Journal*, Vol. 10, No. 11, 1972, pp. 1425–1429.

[81] Fearn, R. L., and Weston, R. P., "Induced Velocity Field of a Jet in a Crossflow," NASA TP-1087, May 1978.

[82] Karagozian, A. R., "An Analytical Model for the Vorticity Associated with a Transverse Jet," *AIAA Journal*, Vol. 24, No. 3, 1986, pp. 429–436.

[83] Su, L. K., and Mungal, M. G., "Simultaneous Measurements of Scalar and Velocity Field Evolution in Turbulent Crossflowing Jets," *Journal of Fluid Mechanics*, Vol. 513, 2004, pp. 1–45.

[84] Broadwell, J. E., and Breidenthal, R. E., "Structure and Mixing of a Transverse Jet in Incompressible Flow," *Journal of Fluid Mechanics*, Vol. 148, 1984, pp. 405–412.

P. Givi
Associate Editor